Three-Dimensional Simulation of a Fluid Catalytic Cracking Riser Reactor

4 AUTHORS, INCLUDING:

Asit Kumar Das
Reliance Industries Limited
89 PUBLICATIONS **193** CITATIONS

SEE PROFILE

Edward Baudrez
Royal Meteorological Institute of Belgium
16 PUBLICATIONS **55** CITATIONS

SEE PROFILE

Geraldine J. Heynderickx
Ghent University
98 PUBLICATIONS **983** CITATIONS

SEE PROFILE

Article

Three-Dimensional Simulation of a Fluid Catalytic Cracking Riser Reactor

Asit K. Das, Edward Baudrez, Guy B. Marin, and Geraldine J. Heynderickx

More About This Article

Additional resources and features associated with this article are available within the HTML version:

- Supporting Information
- Links to the 2 articles that cite this article, as of the time of this article download
- Access to high resolution figures
- Links to articles and content related to this article
- Copyright permission to reproduce figures and/or text from this article

View the Full Text HTML

Three-Dimensional Simulation of a Fluid Catalytic Cracking Riser Reactor

Asit K. Das, Edward Baudrez, Guy B. Marin, and Geraldine J. Heynderickx*

Laboratorium voor Petrochemische Techniek, Ghent University, Krijgslaan 281, S5, B-9000 Gent, Belgium

The three-dimensional simulation of an industrial-scale fluid catalytic cracking riser reactor is performed using a novel density-based solution algorithm. The particle-level fluctuations are modeled in the framework of the kinetic theory of granular flow. The reactor model includes separate continuity equations for the components in the bulk gas and inside the solid phase. The results show a core-annular flow pattern in the major part of the riser with a significant densification of the core region halfway up the riser. The higher solid fraction and a lower solid velocity result in a higher conversion in the annulus region than in the core. However, the concentration profiles of the gaseous components are relatively flat due to the excellent radial mixing in the riser. The radially averaged axial solid velocity shows a considerable slip from the gas phase, amounting to a typical slip factor (ratio of gas/solid axial velocities) of about 2. The high slip factor results from the radial segregation of particles. The simulated product yields using the 3D model are comparable with the plant data. A comparison of the results obtained using the 3D and a 1D simulation model shows that the latter is unable to predict the high slip factor adequately unless the solid particle diameter is significantly altered.

Introduction

Fluid catalytic cracking (FCC) is a major conversion process in modern petroleum refineries worldwide. In this process, heavy petroleum fractions are catalytically cracked to more useful lighter products such as gasoline, middle distillate, LPG, and so forth. Figure 1 shows a schematic diagram of a modern riser type FCC unit. The preheated (330–370 °C) feedstock (boiling range: 370–600 °C) is injected with steam through feed nozzles in the bottom of the riser. The hot catalyst (650–730 °C) is circulated from the regenerator via a standpipe to the bottom of the riser. The atomized feed vaporizes almost instantaneously in contact with the hot regenerated catalyst. The upward velocity of the produced vapor is sufficient to lift the catalyst up along the riser height, where further molar expansion occurs via the catalytic cracking reactions. The coke produced from the cracking reactions in the riser is deposited on the catalyst. At the riser end, the spent catalyst is separated from the vapor.

After steam stripping, the coked catalyst is fed to the regenerator, where the coke is burnt in the presence of air, at a temperature of 650–730 °C. The heat produced from the coke combustion is transported to the riser via the regenerated catalyst circulation. The latter supplies the heat demand (heat of feed vaporization and endothermic heat of cracking) of the riser. Hence, the continuous catalyst circulation between the riser and the regenerator guarantees that the FCC process is automatically heat-balanced.

There is a significant economic incentive in increasing the FCC product yields, even marginally by 1%. The first step is to investigate the mechanism of catalytic cracking reactions and develop suitable kinetic models. These models have varying complexity in defining the feed-product lumps. The simplest model is the 3-lump kinetic model[1] which considers the heavy gas oil, the
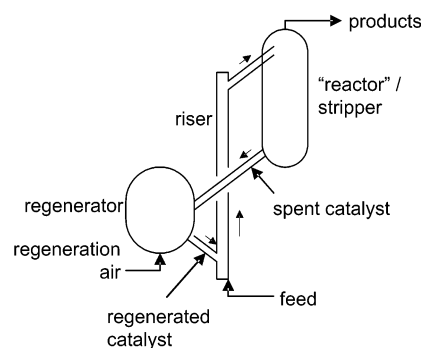

Figure 1. Schematic diagram of an FCC unit.

gasoline, and the remaining components (coke + gas) as the only lumps in the feed. In the 10-lump kinetic model[2] the heavy and middle distillate fractions are each subdivided into four different lumps linked to the chemical nature of the molecules: paraffins P_h, naphthenes N_h, aromatic substituents A_h, and carbon atoms inside the aromatic rings F_h. In contrast to the lump models, a detailed microscopic level definition of the reactions, known as single-event kinetic modeling,[3] permits a detailed description of the catalytic cracking based on the mechanism of the various reactions involving carbenium ions. It may involve thousands of chemical species. However, the coke formation, the catalyst deactivation, and the variation of rate coefficients with catalyst properties are yet to be addressed in the single-event modeling approach.

The other issue in the modeling of riser reactors is the complex hydrodynamics of the gas–solid flow. Hydrodynamic modeling has advanced from 1D simulation of axial profiles[4,5] to the more generalized kinetic theory of granular flow.[6] While many previous FCC simulations are based on complex kinetic models, the hydrodynamics of the riser are oversimplified in most cases, for example, by using a constant slip factor.[7,8] Hence, a complete 3D simulation of flow and reactions in a FCC riser is yet to be performed. Furthermore, most

* To whom correspondence should be addressed. Tel.: +32 9 264 45 32. Fax: +32 9 264 49 99. E-mail: geraldine. heynderickx@rug.ac.be.

of the previous simulations of FCC risers[9,10] are based on the pressure-based solution algorithm. In this work, the density-based algorithm modified for low-velocity two-phase flow[11] will be used for the solution of the model equations. The former involves a multiloop sequential solution of the model equations, while the latter is based on the simultaneous solution of the equations.[12]

Reactor Model Equations

The reactor model equations are subdivided in two blocks: flow and reactions.

Flow model equations:

Continuity equation for the gas phase

$$\frac{\partial}{\partial t}(\epsilon_g \rho_g) + \frac{\partial}{\partial \mathbf{x}} \cdot (\epsilon_g \rho_g \bar{\mathbf{u}}) = \sum_j M_j k_{g_j} a_v (Y_j^s - Y_j) \quad (1)$$

Momentum equations (x,y,z) for the gas phase

$$\frac{\partial}{\partial t}(\epsilon_g \rho_g \bar{\mathbf{u}}) + \frac{\partial}{\partial \mathbf{x}} \cdot (\epsilon_g \rho_g \bar{\mathbf{u}} \bar{\mathbf{u}}) = -\frac{\partial\left(\bar{P} + \frac{2}{3}\rho_g k\right)\delta_{ij}}{\partial \mathbf{x}} -$$

$$\frac{\partial}{\partial \mathbf{x}} \cdot (\epsilon_g \overline{\mathbf{s}_g}) + \epsilon_g \rho_g \mathbf{g} - \beta(\bar{\mathbf{u}} - \mathbf{v}) + \sum_j M_j k_{g_j} a_v (Y_j^s - Y_j)\mathbf{v}$$

$$(2)$$

where

$$\overline{\mathbf{s}_g} = \overline{\mathbf{s}_g^m} + \mathbf{s}_g^t = -\left[\left(\xi_g - \frac{2}{3}\mu_g\right)\left(\frac{\partial\bar{\mathbf{u}}}{\partial\mathbf{x}}\right) + \right.$$
$$\left. (\mu_g + \mu_g^t)\left\{\left(\frac{\partial\bar{\mathbf{u}}}{\partial\mathbf{x}}\right) + \left(\frac{\partial\bar{\mathbf{u}}}{\partial\mathbf{x}}\right)^T\right\}\right]$$

Energy equation for the gas phase

$$\frac{\partial}{\partial t}(\epsilon_g \rho_g \overline{E_g}) + \frac{\partial}{\partial \mathbf{x}} \cdot (\epsilon_g \rho_g \overline{E_g}\bar{\mathbf{u}}) = \frac{\partial}{\partial \mathbf{x}} \cdot \left(\epsilon_g(\lambda + \lambda^t)\frac{\partial\bar{T}}{\partial\mathbf{x}}\right) -$$

$$\frac{\partial}{\partial \mathbf{x}} \cdot \left(\left(\bar{P} + \frac{2}{3}\rho_g k\right)\bar{\mathbf{u}}\right) - \frac{\partial}{\partial \mathbf{x}} \cdot (\epsilon_g \overline{\mathbf{s}_g} \cdot \bar{\mathbf{u}}) - \frac{\beta}{2}(\bar{\mathbf{u}} \cdot \bar{\mathbf{u}} - \mathbf{v} \cdot \mathbf{v}) +$$

$$h_f a_v(T_s - T) + \epsilon_g \rho_g \mathbf{g} \cdot \bar{\mathbf{u}} - \beta\left(k - \frac{3}{2}\theta\right) + \sum_j k_{g} a_v(Y_j^s -$$

$$Y_j)h_{m_j}^s + \sum_j M_j k_{g_j} a_v(Y_j^s - Y_j)\left(\frac{1}{2}\mathbf{v}\cdot\mathbf{v} + \frac{3}{2}\theta\right) \quad (3)$$

Turbulent kinetic energy equation for the gas phase

$$\frac{\partial}{\partial t}(\epsilon_g \rho_g k) + \frac{\partial}{\partial \mathbf{x}} \cdot (\epsilon_g \rho_g \bar{\mathbf{u}} k) = \frac{\partial}{\partial \mathbf{x}} \cdot \left(\epsilon_g \frac{\mu_g + \mu_g^t}{\sigma_k}\frac{\partial k}{\partial\mathbf{x}}\right) +$$

$$\left[\epsilon_g \mu_g^t\left[\left(\frac{\partial\bar{\mathbf{u}}}{\partial\mathbf{x}}\right) + \left(\frac{\partial\bar{\mathbf{u}}}{\partial\mathbf{x}}\right)^T\right]\right] : \left(\frac{\partial\bar{\mathbf{u}}}{\partial\mathbf{x}}\right) - \epsilon_g \rho_g \epsilon - \beta(2k - q_{12}) +$$

$$\sum_j \frac{3}{2}M_j k_{g_j} a_v(Y_j^s - Y_j)\theta \quad (4)$$

Turbulence dissipation equation for the gas phase

$$\frac{\partial}{\partial t}(\epsilon_g \rho_g \epsilon) + \frac{\partial}{\partial \mathbf{x}} \cdot (\epsilon_g \rho_g \bar{\mathbf{u}} \epsilon) = \frac{\partial}{\partial \mathbf{x}} \cdot \left(\epsilon_g \frac{\mu_g + \mu_g^t}{\sigma_\epsilon}\frac{\partial\epsilon}{\partial\mathbf{x}}\right) +$$

$$C_{1\epsilon}\frac{\epsilon}{k}\left[\epsilon_g \mu_g^t\left[\left(\frac{\partial}{\partial\mathbf{x}}\bar{\mathbf{u}}\right) + \left(\frac{\partial}{\partial\mathbf{x}}\bar{\mathbf{u}}\right)^T\right] : \left(\frac{\partial}{\partial\mathbf{x}}\bar{\mathbf{u}}\right)\right] -$$

$$C_{2\epsilon}\epsilon_g \rho_g \frac{\epsilon^2}{k} - \beta(2k - q_{12})C_{4\epsilon}\frac{\epsilon}{k} \quad (5)$$

Continuity equation for the solid phase

$$\frac{\partial(\epsilon_s \rho_{sp})}{\partial t} + \frac{\partial(\epsilon_s \rho_{sp}\mathbf{v})}{\partial\mathbf{x}} = -\sum_j M_j k_{g_j} a_v(Y_j^s - Y_j) \quad (6)$$

Continuity equation for sorbent/catalyst only

$$\frac{\partial(\epsilon_s \rho_s)}{\partial t} + \frac{\partial(\epsilon_s \rho_s\mathbf{v})}{\partial\mathbf{x}} = 0 \quad (7)$$

Momentum equations (x,y,z) for the solid phase

$$\frac{\partial(\epsilon_s \rho_{sp}\mathbf{v})}{\partial t} + \frac{\partial(\epsilon_s \rho_{sp}\epsilon_{sp}\mathbf{v}\mathbf{v})}{\partial\mathbf{x}} = -\frac{\partial P_s}{\partial\mathbf{x}} - \frac{\partial(\epsilon_s \mathbf{s}_s)}{\partial\mathbf{x}} + \epsilon_s \rho_{sp}\mathbf{g} +$$

$$\beta(\bar{\mathbf{u}} - \mathbf{v}) - \sum_j M_j k_{g_j} a_v(Y_j^s - Y_j)\mathbf{v} \quad (8)$$

where

$$\mathbf{s}_s = -\left[\left(\xi_s - \left(\frac{2}{3}\right)\mu_s\right)((\partial/\partial\mathbf{x})\cdot\mathbf{v}) + \mu_s((\partial\mathbf{v}/\partial\mathbf{x}) + (\partial\mathbf{v}/\partial\mathbf{x})^T)\right]$$

Granular temperature equation for the solid phase

$$\frac{3}{2}\left[\frac{\partial}{\partial t}(\epsilon_s \rho_{sp}\theta) + \nabla\cdot(\epsilon_s \rho_{sp}\theta\mathbf{v})\right] = -(P_s\mathbf{I} + \epsilon_s\mathbf{s}_s):\nabla\mathbf{v} -$$

$$\nabla\cdot(\epsilon_s\mathbf{h}) + \beta q_{12} - 3\beta\theta - \gamma - \sum_j \frac{3}{2}M_j k_{g_j} a_v(Y_j^s - Y_j)\theta \quad (9)$$

Gas−solid turbulence correlation

$$\frac{\partial}{\partial t}(\epsilon_s \rho_{sp} q_{12}) + \frac{\partial}{\partial\mathbf{x}}(\epsilon_s \rho_{sp} q_{12}\mathbf{v}) = \frac{\partial}{\partial\mathbf{x}}\cdot\left(\epsilon_s \rho_{sp}\frac{\nu_{12}}{\sigma_q}\frac{\partial q_{12}}{\partial\mathbf{x}}\right) +$$

$$\left[\epsilon_s \rho_{sp}\nu_{12}\left[\left(\frac{\partial}{\partial\mathbf{x}}\bar{\mathbf{u}}\right) + \left(\frac{\partial}{\partial\mathbf{x}}\mathbf{v}\right)^T\right]\right] : \left(\frac{\partial}{\partial\mathbf{x}}\mathbf{v}\right) + \left[\epsilon_s \rho_{sp}\nu_{12}\left[\left(\frac{\partial}{\partial\mathbf{x}}\mathbf{v}\right) + \right.\right.$$

$$\left.\left.\left(\frac{\partial}{\partial\mathbf{x}}\bar{\mathbf{u}}\right)^T\right]\right] : \left(\frac{\partial}{\partial\mathbf{x}}\bar{\mathbf{u}}\right) - \frac{\epsilon_s}{3}\left[\rho_{sp} q_{12}\mathbf{I} + \rho_{sp}\nu_{12}\left[\left(\frac{\partial}{\partial\mathbf{x}}\cdot\mathbf{v}\right) + \right.\right.$$

$$\left.\left(\frac{\partial}{\partial\mathbf{x}}\cdot\bar{\mathbf{u}}\right)\mathbf{I}\right] : \left(\frac{\partial}{\partial\mathbf{x}}\mathbf{v}\right) - \frac{\epsilon_s}{3}\left[\rho_{sp} q_{12}\mathbf{I} + \rho_{sp}\nu_{12}\left[\left(\frac{\partial}{\partial\mathbf{x}}\cdot\bar{\mathbf{u}}\right) + \right.\right.$$

$$\left.\left(\frac{\partial}{\partial\mathbf{x}}\cdot\mathbf{v}\right)\mathbf{I}\right] : \left(\frac{\partial}{\partial\mathbf{x}}\cdot\bar{\mathbf{u}}\right) - \epsilon_s \rho_{sp}\epsilon_{12} - \beta\left(q_{12} + \frac{\epsilon_s\rho_{sp}}{\epsilon_g\rho_g}q_{12} - \right.$$

$$\left. 2k - \frac{\epsilon_s\rho_{sp}}{\epsilon_g\rho_g}3\theta\right) \quad (10)$$

Reaction model equations:

Component continuity equation in gas phase

$$\frac{\partial(\epsilon_g \overline{C_j})}{\partial t} + \frac{\partial}{\partial\mathbf{x}}\cdot(\epsilon_g \overline{C_j}\bar{\mathbf{u}}) =$$

$$k_{g_j}(a_m\epsilon_s\rho_{sp})\left(\frac{RT}{P}\right)(C_j^s - \overline{C_j}) + \frac{\partial}{\partial\mathbf{x}}\left[\left(D_m + \frac{\nu_g^t}{\sigma_c}\right)\epsilon_g\frac{\partial\overline{C_j}}{\partial\mathbf{x}}\right] \quad (11)$$

Component continuity equation for gas inside solid phase

$$\frac{\partial(\epsilon_s \epsilon_g^s C_j^s)}{\partial t} + \frac{\partial}{\partial\mathbf{x}}\cdot(\epsilon_s \epsilon_g^s C_j^s\mathbf{v}) = k_{g_j}(a_m\epsilon_s\rho_{sp})\left(\frac{RT}{P}\right)(\overline{C_j} - C_j^s) +$$

$$\mathscr{R}_f\epsilon_s\rho_s + \frac{\partial}{\partial\mathbf{x}}\left[\left(\epsilon_s\epsilon_g^s\frac{\nu_s}{\sigma_s}\right)\frac{\partial C_j^s}{\partial\mathbf{x}}\right] \quad (12)$$

Surface species continuity equation in solid phase

$$\frac{\partial(\epsilon_s \rho_{sp} \Theta_l)}{\partial t} + \frac{\partial}{\partial \mathbf{x}} \cdot (\epsilon_s \rho_{sp} \Theta_l \mathbf{v}) = \frac{\partial}{\partial \mathbf{x}} \left[\left(\epsilon_s \rho_{sp} \frac{\nu_s}{\sigma_\Theta} \right) \frac{\partial \Theta_l}{\partial \mathbf{x}} \right] + \mathscr{R}_l \epsilon_s \rho_s \tag{13}$$

It is seen that the model equations are based on the Eulerian–Eulerian approach. The gas-phase equations are time-smoothed; the solid-phase equations, however, are only locally averaged. Hence, the set of model equations is of the turbulent gas/laminar solid type and is applied to obtain the mean values of the solid-phase properties. Related constitutive equations for the solid-phase pressure, viscosity, stress, and so forth are discussed by De Wilde et al.[11]

For modeling the gas-phase turbulence, the well-known $k-\epsilon$ model (eqs 4 and 5) is used with additional turbulence exchange terms due to gas–solid drag. On the other hand, the solid-phase flow is assumed to be laminar and modeled using the *kinetic theory of granular flow* (KTGF), resulting in the well-known granular temperature equation, eq 9. These equations involve a gas–solid turbulence correlation term q_{12}, which is defined as the scalar multiplication of the fluctuating velocities of gas and particle. In this work, q_{12} is modeled using a semiempirical equation, eq 10, taken from the work of Simonin.[13]

The kinetic theory of granular flow[6] (KTGF) models the binary particle–particle collisions, but does not account for the mesophase fluctuations due to clustering in the solid phase. The clustering of particles is unavoidable at higher solid fluxes, especially with Geldart A particles such as FCC powders. Hence, the validity of KTGF at higher solid fluxes is yet to be established. In the present model, the interphase turbulence exchange terms $\beta[q_{12} - 3\theta]$ are removed from the granular temperature equation, eq 9. Similar terms in the $k-\epsilon$ equations, eqs 4 and 5, are also neglected. Hence, there is no need to solve the q_{12} equation, eq 10. Such simplifications are justified from the results of Agrawal et al.[14] who have used a fine grid (1 mm) while investigating the effect of grid size on the magnitude of the interphase fluctuating motion exchange terms. They have shown that the dissipation through these interphase exchange terms $\beta[q_{12} - 3\theta]$ is nearly compensated for by an increase in the granular temperature production due to additional shear in the solid phase caused by the turbulent motion of particles, when the simulation is performed on a fine grid. Since the latter effect cannot be computed accurately in a coarse grid simulation, it was found that neglecting the above exchange terms indeed provides a more reliable prediction of the flow fields.[15] Extending the same reasoning to the dissipation of granular temperature by inelastic collisions (γ in eq 9), the particle–particle collisions can be assumed as perfectly elastic (restitution coefficient $e = 1$) in a coarse grid simulation since the unrealistic sensitivity of the flow fields on the value of e is related to the coarse nature of the grid.[14]

Furthermore, it is shown later in the sections "Validation of the Gas–Solid Turbulence Model" and "Radial and Axial Variations of Flow and Reaction Variables" of this work that the KTGF-based turbulence model with the above simplifications leads to a reliable simulation of flow fields over a broad range of operating conditions, especially when the mass flux of the solid is moderately high, as in the case of the FCC riser conditions adopted in this work.

Note that the solid-phase energy equation, although it is present in the code, is not solved and therefore not reproduced here. This issue, and the underlying reason, is discussed in "Energy Equations" under "Numerical Aspects".

Kinetic Model

Considering the simplicity of the 3-lump modeling[1] and the complexity of the single-event modeling,[3] a compromise is chosen. Since the primary objective is to study the effect of the flow on the reaction variables, a 12-lump kinetic model[16] is adopted in this work. It is shown in Figure 2. The stoichiometric factor of a lump j in path p can be generally expressed as

$$\gamma_{jp} = \delta_{ij} \frac{M_i}{M_j} \tag{14}$$

where i is the reactant lump number in path p, M is the molecular mass of the lump, and $\delta_{ij} = 0$ if path p is not linked to lump j (Figure 2); $\delta_{ij} = 1$ if $j > i$ and $\delta_{ij} = -1$ if $j = i$.

The deposition of coke on the catalyst surface significantly decreases the catalyst activity. Although the product selectivity is also affected to some extent, the latter effect is neglected in most of the cases. In this work, the catalyst activity is related to the coke content; that is, the mass fraction of coke on the catalyst C_c is calculated in accordance with the equation[9]

$$\varphi_c = (1 + 51.0 C_c)^{-2.78} \tag{15}$$

Following the kinetic scheme shown in Figure 2, it is possible to express the net production rate of a component j based on the reaction rate of the individual steps

$$\mathscr{R}_j = \sum_{p=1}^{N} \gamma_{jp} r_p \tag{16}$$

where N is the total number of reaction paths. The individual reaction rate r_p is a function of concentration and catalyst activity

$$r_p = k_p e^{(-E_p/R)[(1/T)-(1/T_b)]} \varphi_{F_h} \varphi_c C_p^s \tag{17}$$

where C_p^s is the concentration of the reactant lump in path p and superscript s refers to the gas inside the solid phase; k_p is the rate coefficient for path p at a base temperature T_b. The values of the kinetic parameters for the 12-lump model are shown in Table 1 for a base temperature of 773 K. In eq 17, the factor φ_{F_h} accounts for the change in the free site concentration due to the adsorption of heavy aromatic rings F_h on the catalyst surface.[2] Assuming the adsorption to be in equilibrium[17] results in

$$\varphi_{F_h} = \frac{1}{1 + K_h C_{F_h}^s} \tag{18}$$

where K_h is the equilibrium adsorption coefficient of lump F_h. However, this effect is negligible when the concentration of F_h is small. Following eq 16 and Figure
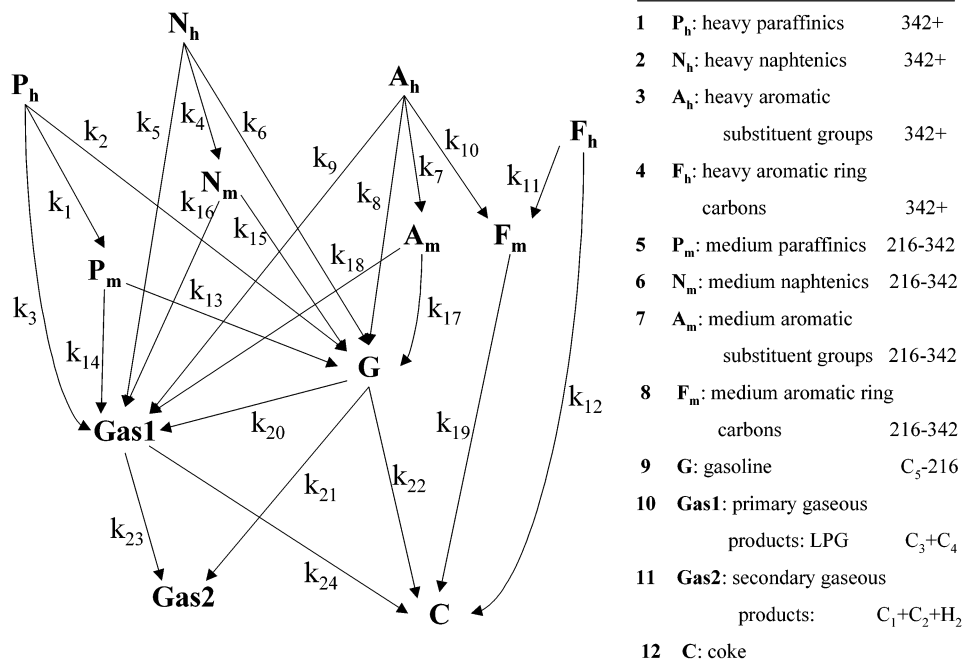
Lump No.	Lump	Boiling range, °C
1	P_h: heavy paraffinics	342+
2	N_h: heavy naphtenics	342+
3	A_h: heavy aromatic substituent groups	342+
4	F_h: heavy aromatic ring carbons	342+
5	P_m: medium paraffinics	216-342
6	N_m: medium naphtenics	216-342
7	A_m: medium aromatic substituent groups	216-342
8	F_m: medium aromatic ring carbons	216-342
9	G: gasoline	C_5-216
10	Gas1: primary gaseous products: LPG	C_3+C_4
11	Gas2: secondary gaseous products:	C_1+C_2+H_2
12	C: coke	

Figure 2. Reaction network of the 12-lump FCC kinetic model.[16]

Table 1. Kinetic Parameters of the 12-Lump FCC Model[16]

path number (Figure 2) p	rate coefficient[a] k_p, 10^{-3} m³ kg$_{cat}^{-1}$ s^{-1}	activation energy[b] E_p, kJ mol^{-1}	path number (Figure 2) p	rate coefficient[a] k_p, 10^{-3} m³ kg$_{cat}^{-1}$ s^{-1}	activation energy[b] E_p, kJ mol^{-1}
1	2.38	21.0	13	2.3	37.8
2	5.28	21.0	14	1.97	37.8
3	0	21.0	15	18.3	37.8
4	6.25	21.0	16	2.27	37.8
5	4.13	21.0	17	0.51	75.6
6	23.5	21.0	18	1.0	75.6
7	5.27	58.8	19	0.28	75.6
8	17.5	58.8	20	0.65	84.0
9	9.5	58.8	21	0	84.0
10	13.8	58.8	22	0	84.0
11	1.62	58.8	23	0.61	105.0
12	4.06	29.4	24	1.35	105.0

[a] Data from Peixoto and de Medeiros.[16]   [b] Data from Jacob et al.[2]

2, the net production rate of a lump, for example, P_m, is expressed as

$$\mathcal{R}_{P_m} = [\gamma_{51} k_1 e^{(-E_1/R)[(1/T_b)-(1/T)]} C_{P_h}^\mathfrak{s} -$$
$$k_{14} e^{(-E_{14}/R)[(1/T_b)-(1/T)]} C_{P_m}^\mathfrak{s} -$$
$$k_{13} e^{(-E_{13}/R)[(1/T_b)-(1/T)]} C_{P_m}^\mathfrak{s}] \varphi_c \varphi_{F_h} \quad (19)$$

where $\gamma_{51} = M_{P_h}/M_{P_m}$.

Accordingly, the gas phase consists of lumps 1−11 (as shown in Figure 2) and steam, totaling 12 components. Similarly, the gas inside the solid phase also has 12 components. The only surface species considered is coke.

Initial and Boundary Conditions

For the reaction model equations (eqs 11−13), it is necessary to define the inlet concentration of the gaseous components as well as the coke on the regenerated catalyst. The component concentration C_j in the bulk of the gas phase is calculated from the feed composition and other inlet conditions as

$$C_j = Y_j \left(\frac{P}{RT}\right) \quad (20)$$

The inlet concentration $C_j^\mathfrak{s}$ inside the solid phase is based on the assumption that the regenerated catalyst pores are filled with steam only. The coke content of the regenerated catalyst is assumed to be zero. Other inlet conditions such as feed rate and catalyst circulation rate, are summarized in Table 2. The inlet conditions mostly correspond to a case study reported by Gao et al.[9] for an industrial FCC unit running at moderate severity. Certain values such as outlet pressure are assumed since they are not reported in this case study. In addition, the outlet configuration adopted in this work is an abrupt T-type outlet as compared to a smooth top outlet in the case study. The T-type outlet is adopted to study the impact of the side outlets on the flow and reaction variables. Note that the catalyst-to-oil ratio is somewhat lower than the typical value of 5−8 in most of the commercial FCC units.

Numerical Aspects

Pressure- and Density-Based Solution Methods. In general, there are two approaches to solving the

Table 2. FCC Riser Dimensions and Operating Conditions Used in the Simulation[9]

property/parameter	symbol	unit	value
riser height	H	m	27.35
riser diameter	D	m	0.4
outlet elevation	H_{out}	m	26.83
total outlet surface area	S_{out}	m^2	0.16^b
particle diameter	d_p	μm	65
particle density	ρ_p	kg m^{-3}	1500
restitution coefficient	e		1.0
wall restitution coefficient	e_w		0.9
inlet			
$\quad$ solid volume fraction	ϵ_{inb}		0.0816
$\quad$ solid flux	G_s	kg m^{-2} s^{-1}	79.0
$\quad$ average gas velocity	$u_{g,avg}$	m s^{-1}	4.55
$\quad$ granular temperature	θ	m^2 s^{-2}	0.14^b
$\quad$ gas turbulent intensity^a			0.02
$\quad$ feed temperature	T_g	K	698
$\quad$ catalyst temperature	T_s	K	875
$\quad$ feed mass flow rate		kg s^{-1}	2.68
$\quad$ steam mass flow rate		kg s^{-1}	0.047
$\quad$ catalyst mass flow rate		kg s^{-1}	9.93
$\quad$ C/O			3.7
inlet feed composition		mole fraction	
$\quad$ P_h			0.50
$\quad$ N_h			0.06
$\quad$ A_h			0.13
$\quad$ F_h			0.05^b
$\quad$ steam			0.26
outlet pressure	P	10^5 Pa	1.013^b

^{a} Gas turbulent intensity is defined as $\sqrt{2k/3}/|\bar{\mathbf{u}}|$. ^{b} Assumed value.

governing conservation equations: pressure-based and density-based solution methods. In pressure-based methods, pressure and velocity are calculated separately in an iterative manner from the continuity and momentum balance equations. However, in density-based methods, all model equations are solved simultaneously and the corrected values of all dependent variables for the next time step are obtained directly; no iterations are needed to satisfy both pressure and momentum. Furthermore, the convergence speed in the latter method can be enhanced by applying preconditioning, described below. For more details on the comparison of the above two methods, reference is made to our previous work on the subject.[18]

Derivation of the Algebraic Set of Equations. All governing differential equations (the flow equations, eqs 1−10, and the reaction equations, eqs 11−13) can be cast in the following generic form

$$\frac{\partial \mathbf{Q}}{\partial t} + \frac{\partial}{\partial \mathbf{x}} \cdot \boldsymbol{\varphi} = \mathbf{S} \qquad (21)$$

where $\mathbf{Q}$ represents the vector of all conservative variables (as opposed to the vector $\mathbf{W}$ of primary variables such as gas-phase pressure and density, x,y,z-components of velocity, etc.), $\boldsymbol{\varphi}$ represents the flux vector of these variables, containing the convective and acoustic fluxes as well as the viscous fluxes, and $\mathbf{S}$ represents the vector of source terms.

In the interest of simplicity, the following discussion is restricted to the flow equations in the absence of source terms. In this case, eq 21 reduces to

$$\frac{\partial \mathbf{Q}}{\partial t} + \frac{\partial}{\partial \mathbf{x}} \cdot \boldsymbol{\varphi} = 0 \qquad (22)$$

with $\mathbf{Q}$ given by

$$\mathbf{Q}^{\mathrm{T}} =$$

$$(\epsilon_s \rho_s \quad \epsilon_s \rho_{sp} \quad \epsilon_g \rho_g \quad \epsilon_s \rho_{sp} v_x \quad \epsilon_s \rho_{sp} v_y \quad \epsilon_s \rho_{sp} v_z \quad \epsilon_g \rho_g u_x \quad \cdots$$
$$\cdots \quad \epsilon_g \rho_g u_y \quad \epsilon_g \rho_g u_z \quad \epsilon_g \rho_g E_g \quad {}^3/_2 \epsilon_s \rho_{sp} \theta \quad \epsilon_g \rho_g k \quad \epsilon_g \rho_g \epsilon \quad \epsilon_s \rho_{sp} q_{12})$$
$$(23)$$

In the finite volume approach, the conservation equations, eq 22, are formally integrated over an arbitrary control volume V. After applying the divergence theorem, this results in

$$\frac{\partial}{\partial t} \iiint_V \mathbf{Q} \, dV + \iint_S \boldsymbol{\varphi} \cdot \mathbf{n} \, dS = 0 \qquad (24)$$

$\mathbf{n}$ being the normal vector of each interface.

In this work, a dual time-stepping approach is adopted, where eq 24 is replaced by

$$\frac{\partial}{\partial \tau} \iiint_V \mathbf{Q} \, dV + \frac{\partial}{\partial t} \iiint_V \mathbf{Q} \, dV + \iint_S \boldsymbol{\varphi} \cdot \mathbf{n} \, dS = 0 \qquad (25)$$

in which τ represents pseudo-time rather than real time, which is denoted by t. τ is introduced to be able to solve eq 24 for $\mathbf{Q}$ in an iterative manner, starting from a known value at time t and ultimately yielding a value at time $t + \Delta t$. Pseudo-time bears no resemblance to real time and is only a means of obtaining successively better estimates of the solution of eq 24. Once convergence is achieved, the pseudo-time derivative in eq 25 vanishes. Steady-state calculations can also be performed using eq 25, by setting Δt equal to a large value (say 5000 s), effectively reducing eq 25 to a single time-stepping form involving only pseudo-time.

An additional advantage of the dual time-stepping approach is that the pseudo-time derivative can be multiplied with a preconditioning matrix $\boldsymbol{\Gamma}$ without affecting the time accuracy of the solution. The main incentive for introducing preconditioning is that it enhances the convergence speed. This is described in greater detail later in the text.

Next, the preconditioned dual time-stepping equation is discretized in time and space for a particular grid point i with the surrounding grid points indicated by i', yielding

$$\boldsymbol{\Gamma} \frac{\Delta t}{\Delta \tau}(Q_i^{(m+1)} - Q_i^{(m)}) + (Q_i^{(m+1)} - Q_i^{(t)}) + \Delta t \cdot (A_{i'}^{(m)} Q_{i'}^{(m)} - A_i^{(m)} Q_i^{(m+1)}) = 0 \quad (26)$$

In this equation, superscripts (m) and $(m + 1)$ denote successive estimates for $\mathbf{Q}$ at time level $t + \Delta t$, while the superscript (t) is used to represent the (known) value of $\mathbf{Q}$ at time t. The flux term is symbolically expressed as the difference of contributions from the current grid point and surrounding grid points.

Isolating all contributions that pertain to the new estimate (pseudo-time level $m + 1$) in the left-hand side of eq 26, one obtains

$$\left(\boldsymbol{\Gamma}\frac{\Delta t}{\Delta \tau} + \mathbf{I} - A_i^{(m)}\right)(Q_i^{(m+1)} - Q_i^{(m)}) = -(Q_i^{(m)} - Q_t^{(t)} + \Delta t \cdot (A_{i'}^{(m)} Q_{i'}^{(m)} - A_i^{(m)} Q_i^{(m)})) \quad (27)$$

a form that readily reduces to

$$\tilde{A}_i^{(m)} \Delta Q_i = \tilde{B}_i^{(m)} \qquad (28)$$

where $\Delta \mathbf{Q}$ is shorthand for $Q_i^{(m+1)} - Q_i^{(m)}$. Equation 28 in fact represents a set of algebraic equations in the conservative variables contained within $\mathbf{Q}$ (eq 23). This set of equations is currently solved using Gauss' elimination method. Note that all quantities that are treated in an implicit way will give rise to a contribution in the left-hand side of eq 27. As all values related to grid point i and all negative source terms are currently treated that way, the method can be qualified as a point-implicit method. The surrounding grid points have their values evaluated at pseudo-time level m so that the set of equations, eq 28, can be solved pointwise.

The discretization procedure for the reaction model equations, eqs 11–13, is similar.

For more details on the derivation of eq 28, including a full treatment of the flux discretization and the preconditioning matrix, the reader is referred to the work of De Wilde[19] and De Wilde et al.[11]

Preconditioning. In density-based solution methods using time marching, all variables are solved for simultaneously. Such a method faces the difficulty of a large imparity of the eigenvalues, arising from the difference between the convective and acoustic speeds at low speed flows such as in FCC risers. This is successfully resolved by multiplying the pseudo-time derivative term in eq 25 with a preconditioning matrix $\boldsymbol{\Gamma}$, as mentioned earlier.

$\boldsymbol{\Gamma}$ is formulated such that the acoustic speed is replaced by a reference speed. The latter is scaled according to the convective speed. The reference velocity is defined as[20]

$$U_r = |\mathbf{u}| + 2\frac{(\mu_g + \mu_g^t)}{\rho_g}\left(\frac{1}{\Delta x} + \frac{1}{\Delta y} + \frac{1}{\Delta z}\right) \qquad (29)$$

The transformation matrix $\partial \mathbf{Q}/\partial \mathbf{W}$ is then adapted accordingly by replacing the matrix element

$$K_1 = \frac{\partial \rho_g}{\partial P} = \frac{1}{RT} = \frac{\gamma}{C_g^2} \qquad (30)$$

controlling the acoustic speed, by a term

$$T_1 = \frac{1}{(\alpha U_r)^2} + \frac{1}{c_p^g T} \qquad (31)$$

In eq 31, the scaling factor α is usually equal to 1 in the preconditioning formulation for single-phase flow[20] using the flux difference splitting method. De Wilde et al.[11] recently extended this preconditioning approach to two-phase flow, which is used in this work also, except for a different value of α. Since the acoustic speed is significantly decreased in the presence of solid particles,[21] it was observed that a higher value of α (say 18) is needed to avoid overconditioning of the eigenvalues.[18]

Flow and Reaction Blocks. The flow and reaction equations are integrated separately in two different blocks (see Figure 3). Steady-state computation is performed for both blocks. Starting from the initialized fields, the flow block is integrated first, in a pointwise manner for the entire domain following pseudo-time marching until a steady-state solution is reached. The reaction block equations are integrated next, based on
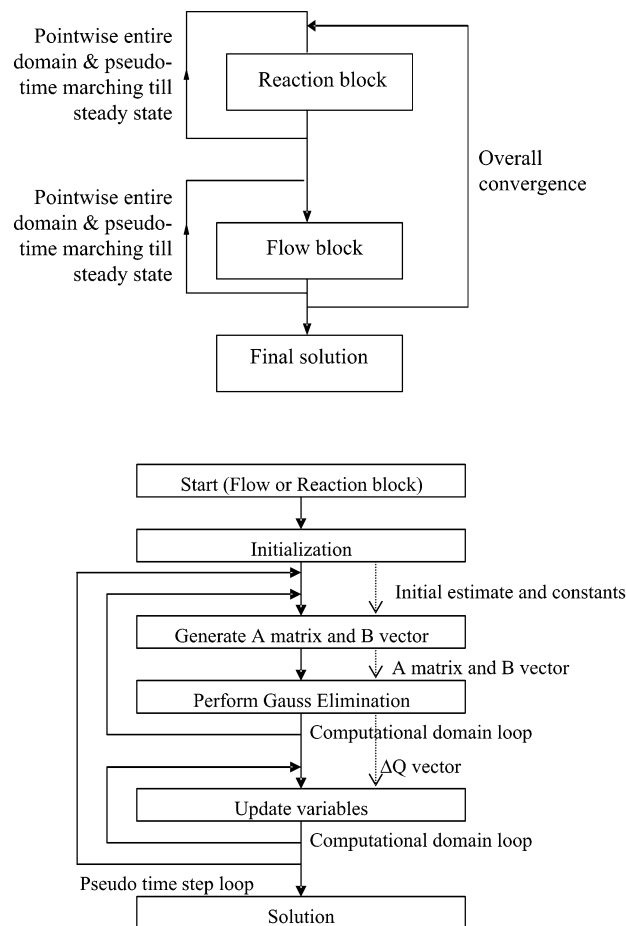

Figure 3. Steady-state separate solution of reaction and flow block followed by an overall loop convergence.

the previously calculated values of the flow variables. The calculation of flow and reaction blocks are then repeated until overall convergence is reached for the variables of both blocks.

Computational Grid. The entire riser height is divided into 67 horizontal layers, placed in a nonuniform manner with a higher grid density near the bottom and the top of the riser. In each horizontal layer, 188 nodes are placed by following a mixture of the Cartesian and the radial coordinates.[11] The average grid spacing in the radial and tangential directions is about 2–3 cm, and in the vertical direction about 30–50 cm. Near the bottom and top section of the riser, the vertical grid spacing is smaller (10–15 cm) to provide a better resolution of the computed profiles. Due to strong inlet/outlet effects, maximum variation in the flow and reaction variables usually occur in these sections of the riser. The above grid spacing is similar to that used in contemporary works (e.g., Gao et al.[9]).

Energy Equations. The temperature profiles for gas and solid phases are imposed to avoid the iterative solution of the solid-phase energy equation since the solid-phase internal energy e_{sp} is a nonlinear function of the temperature T_s, arising from the nonlinear variation of the specific heats of gas and solid with temperature. The gas-phase energy equation, in contrast, is solved and used for the calculation of gas-phase pressure.[18]

The imposed gas- and solid-phase temperatures are shown in Figure 4. The radial temperature variation of both phases is neglected and the axial temperature
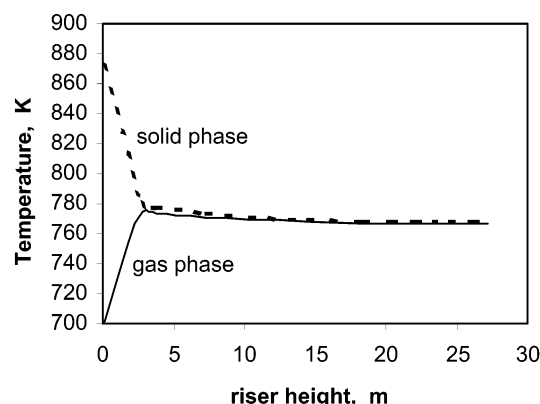
Figure 4. Imposed temperature profiles for gas and solid phases for the 3D simulation. Radial variation of temperature is neglected.

variations due to the endothermicity of the cracking reactions are obtained from a 1D model, described later. The initial temperature gradients are estimated from the simulation data of Theologos and Markatos.[10] The temperature profiles shown in Figure 4 correspond to the average axial temperature profiles of gas and solid in the work of Gao et al.[9] for the majority of the riser. The maximum variation of the temperature for both phases occurs near the entry zone. It may be noted that, for a complete simulation of the entry zone temperature profiles, it is necessary to remember that the feedstock is injected in the liquid phase. However, if instantaneous vaporization of the feedstock is assumed, a gas−solid two-phase model as adopted in this work can be applied. In the latter, it is not possible to specify the actual liquid feed and catalyst temperature at the inlet of the riser. Hence, predicting the actual temperature distribution, especially at the bottom of the riser, requires a detailed three-phase calculation involving the feedstock atomization and its effect on the rate of vaporization.

As the solid-phase energy equation is not solved, the influence of reaction heat, interphase heat transfer, and radial temperature variation are not directly accounted for. The first and second effect are indirectly introduced through the imposed temperature profiles. The gas- and solid-phase temperature gradients in the entry zone of the riser, where interphase heat-transfer effects are important, are obtained from calculations[10] that took heat exchange between gas and solid into account. The remaining temperature data are obtained from the 1D model calculations. In the latter model, the heat effect of the cracking reactions is taken into account. It has to be stressed, however, that our ultimate goal is to solve *all* equations and to compute the aforementioned effects a priori.

Convergence and CFL Number. Two typical residual curves as a function of pseudo-time are presented in Figure 5. A major issue in achieving a stable convergence when solving the flow and reaction blocks separately is the strong coupling between flow and reaction variables. For example, the source term in reaction equation eq 11 is a function of the flow variables temperature, pressure, and solid density $\epsilon_s\rho_{sp}$. Conversely, most of the flow model equations depend on the mole fractions. On solving of the equations of one block, the variables of the other block are treated as constants, ignoring the important interactions between them (e.g., molar expansion caused by the cracking reactions). This approach leads to an instability of the
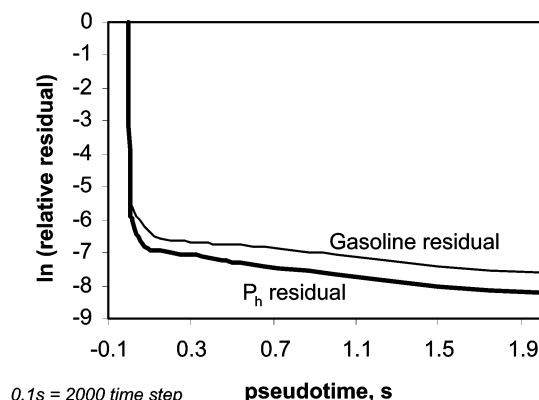

Figure 5. Convergence behavior of paraffin and gasoline residual.

Table 3. Summary of Riser Design and Operating Conditions Used for the Validation of the Turbulence Model

source of experimental data	symbol	units	Godfroy et al.[22]	Sun and Gidaspow[23]
riser height	H	m	12.2	12.2
riser diameter	D	m	0.4	0.2
total outlet surface area	S_{out}	m^2	0.12	0.037
particle diameter	d_p	μm	120	76
particle density	ρ_p	kg m^{-3}	2600	1712
inlet				
solid fraction	ϵ_{inb}		0.0192	0.0286
solid flux	G_s	kg m^{-2} s^{-1}	50.0	489.0
average gas velocity	$u_{g,avg}$	m s^{-1}	4.2	11.0
outlet pressure	P	Pa	101300	101300

convergence, resulting in a severe restriction of the allowable pseudo-time step size. Hence, in the density-based algorithm, it is preferable to solve both flow and reaction equations simultaneously in a single block, a subject of future research.

A typical pseudo-time step of 2.0×10^{-4} s is adopted for the calculations, which corresponds to a CFL (Courant−Friedrich−Lewy) number of 0.2. The low value of the CFL number (normally about 1 for a semi-implicit approach and more than 50 for an implicit approach) is mainly due to the inability of the current algorithm to overcome the strong coupling of flow and reaction variables. For nonreactive flow simulations, the density-based solution method with matrix preconditioning allows the time step to be at least 1 magnitude larger than the corresponding pressure-based solution method.

Validation of the Gas−Solid Turbulence Model

The turbulence model adopted in this work is first validated with the cold-flow experimental data of Godfroy et al.[22] and of Sun and Gidaspow.[23] The operating conditions and riser geometry for both cases are summarized in Table 3. The data of Godfroy et al.,[22] on one hand, correspond to the conditions of a circulating fluidized boiler (CFB) operating with Geldart B particles at moderate solid fluxes. The data of Sun and Gidaspow,[23] on the other hand, correspond to the conditions of a typical FCC plant riser with high solid flux (489 kg m^{-2} s^{-1}).

The measured and simulated axial solid mass flux at 6.6 m elevation for the data of Godfroy et al.[22] are shown in Figure 6(i). The present model is able to predict the
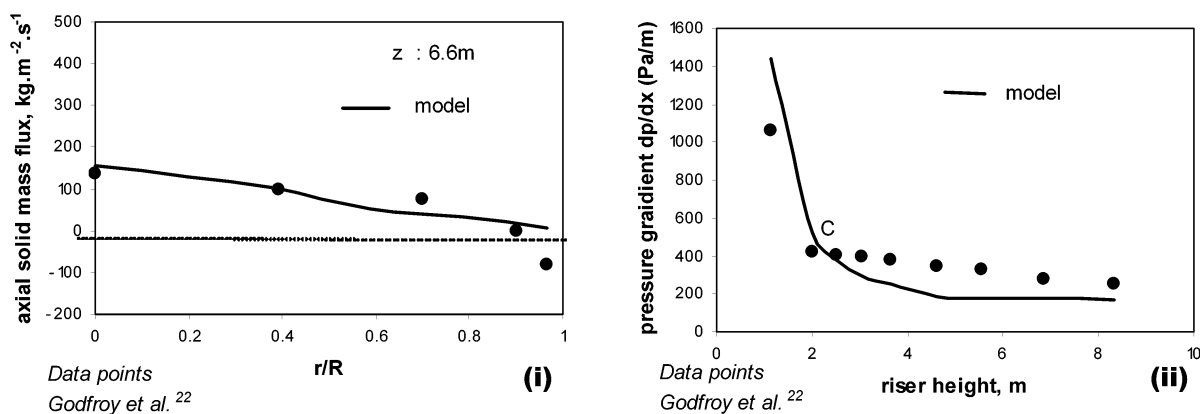
Figure 6. Validation of the turbulence model with data of Godfroy et al.[22] (i) Radial variations of axial solid mass flux. (ii) Axial variation of the pressure gradient. Data correspond to Table 3 and steady-state simulation. G_s = 50.0 kg m^{-2} s^{-1}; u_g = 4.2 m s^{-1}.
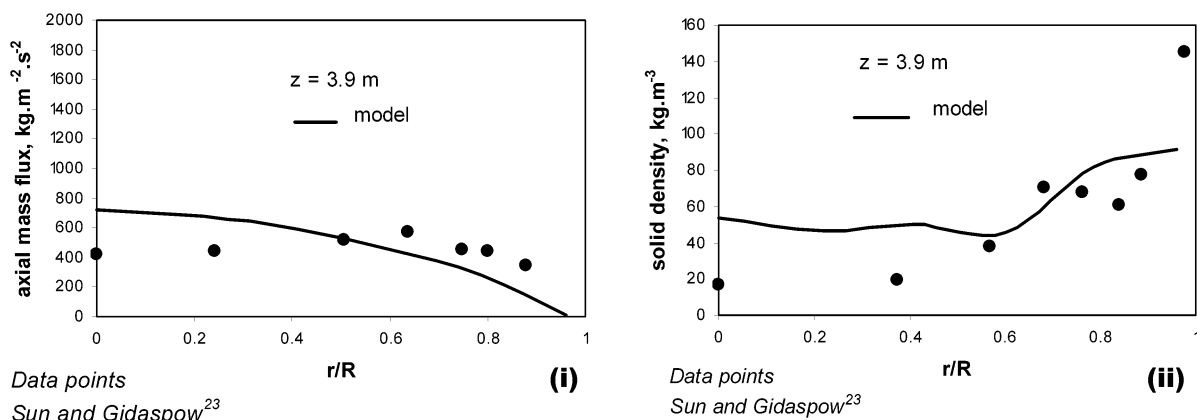

Figure 7. Validation of the turbulence model with data of Sun and Gidaspow.[23] Radial variations of (i) axial solid mass flux and (ii) solid density. Data correspond to Table 3 and steady-state simulation. G_s = 489.0 kg m^{-2} s^{-1}; u_g = 11.0 m s^{-1}.

axial solids mass flux quite accurately, except in the region near the wall. The model variation near the wall is attributed to the following: (i) the use of a universal wall function, (ii) the insufficient number of grid points, and (iii) the absence of modeling of the segregation of larger particles near the wall. The correspondence between the measured and calculated axial pressure gradient for the same case (Godfroy et al.[22]), as shown in Figure 6(ii), demonstrates the applicability of the present gas–solid turbulence model for CFB conditions. The model predicts the pressure drop in the initial acceleration zone quite well, although there is some underprediction in the fully developed region. The latter is mainly attributed to the inadequacy of the present model to account for the effect of clustering of particles on the gas–solid drag.

The axial solid mass flux and solid density for another case (data from Sun and Gidaspow[23]) are shown in Figure 7(i) and (ii), respectively. The model predicts the radial variation of the solid density well except near the wall, due to the reasons explained earlier. Similarly, the axial solids flux is qualitatively predicted, although the location of maximum flux away from the center is not predicted by the model.

The above examples and case studies done at other conditions (not shown here) allow us to conclude that the present turbulence model, even without detailed accounting of the particle clustering effect and nonelastic particle collisions, has the capability to predict the general trend of the hydrodynamic behavior of circulating fluidized beds over a wide range of conditions.

Table 4. Predicted vs Actual Product Yields at the Riser Exit (Averaged over Both Outlets)

product yields[a]	this work[b]	Gao et al.[9,c]	plant
total heavy	39.8	40.5	40.4
paraffinic	35.3		
naphthenic	0.7		
aromatic substituents	0.6		
aromatic ring carbon	3.2		
total middle	16.2	17.2	18.8
paraffinic	8.3		
naphthenic	0.6		
aromatic substituents	2.1		
aromatic ring carbon	5.2		
gasoline	35.0	32.3	29.7
total gas	7.0	6.4	7.8
LPG	6.5		
dry gas	0.5		
coke	2.0	3.6	3.3

[a] Yields are based on wt % of total hydrocarbon. [b] Using kinetic theory of granular flow (KTGF) and density-based solution method. [c] Using $k-\epsilon-k_p$ model and pressure-based solution method.

Comparison of Simulated and Experimental Product Yields

In Table 4, the product yields obtained from the 3D simulation in the present work are compared with available plant data and simulation results.[9] The products yields are averaged over both the outlets. Note that the simulation of Gao et al.[9] is largely based on the $k-\epsilon-k_p$ turbulence model for the solid phase using a pressure-based solution method. On the other hand, the
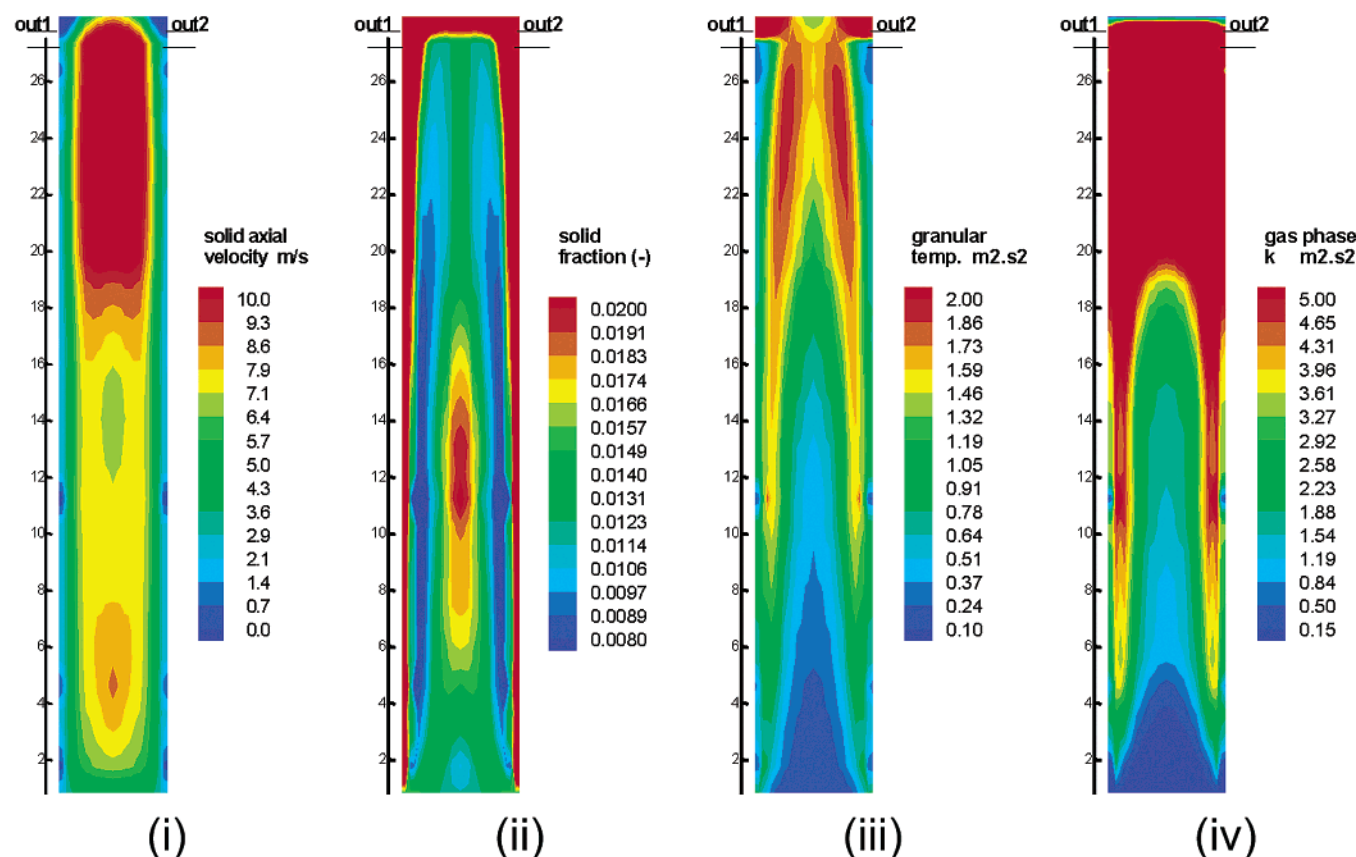
Figure 8. Contour plots of flow variables in a cross section through the outlets. Steady-state simulation. $G_s = 79.0$ kg m^{-2} s^{-1}; $u_g = 4.55$ m s^{-1}; $\theta_{in} = 0.14$ m^2 s^{-2}.

present work is based on the kinetic theory of granular flow and a novel density-based solution algorithm is used.

The product yields are calculated from

$$Z_j = \frac{W_{f} \epsilon_g \rho_g u_z}{C_C \epsilon_s \rho_{sp} v_z + \sum_{j}^{m-1} (W_{f} \epsilon_g \rho_g u_z)} \qquad (32)$$

and are expressed in terms of the weight fractions of hydrocarbons including coke. The product yields obtained in the present simulation are close to the plant data. However, the gasoline yield is generally higher and the coke yield is somewhat lower in the present work as compared to the plant values. The higher gasoline yield in the present simulation is attributed to the outlet effect. An abrupt T-outlet as used in the present simulation results in a higher solid fraction in the top section of the riser. On the other hand, the plant has a smooth outlet at the top. The lower coke yield in the present simulation can be attributed to the imposed value of the F_h lump concentration at the inlet (see Table 2). Hence, considering these facts, the agreement between the product yields in the present simulation and the plant data is reasonable.

Radial and Axial Variations of Flow Variables

The axial and radial variations of the solid volume fraction, the solid axial velocity, the granular temperature, and the gas-phase turbulence are shown in the contour plots of Figure 8. The radial solid fraction,

granular temperature, and solid velocity plots shown in Figure 9 resemble a core-annular flow pattern.

These profiles, especially the solid volume fraction as shown in Figure 9(i), are generally comparable to the profiles reported by Gao et al.[9] Similar core-annular flow is also reported by Landeghem et al.[24] in an experimental study of a cold flow setup having an average gas velocity of 6.7 m s^{-1} and a solid flux of 303 kg m^{-2} s^{-1}. Note that the annulus thickness is significantly higher at the top of the riser as indicated by a higher solid fraction at 24.5 m elevation (Figure 9(i)). This is also clearly seen in Figure 8(ii), where a much larger annulus thickness is seen in the top section of the riser. This is a direct consequence of the T-outlet effect that allows a considerable increase in the solid fraction as reported also by Martin et al.[7]

It is important to note that the flow fields are solved using the steady-state computational mode. This implies that the effects of mesophase fluctuations of the solid due to clustering, especially on the drag force, are not accounted for as such. Despite this, the simulated flow fields are comparable to those measured in a plant. This could be due to the relatively lower solid flux of 80 kg m^{-2} s^{-1} in the present test case as compared to the solid flux of 500 kg m^{-2} s^{-1} in a typical FCC unit. A lower solid flux generally implies lower mesophase fluctuations due to clusters.

The other important point is the sudden increase of the solid fraction in the core region at an elevation of 10.5 m (see Figure 8(ii)). This is mainly attributed to the relatively lower granular temperature in the center at 10.5 m elevation (see Figures 8(iii) and 9(ii)). A lower granular temperature implies a lower fluctuating veloc-
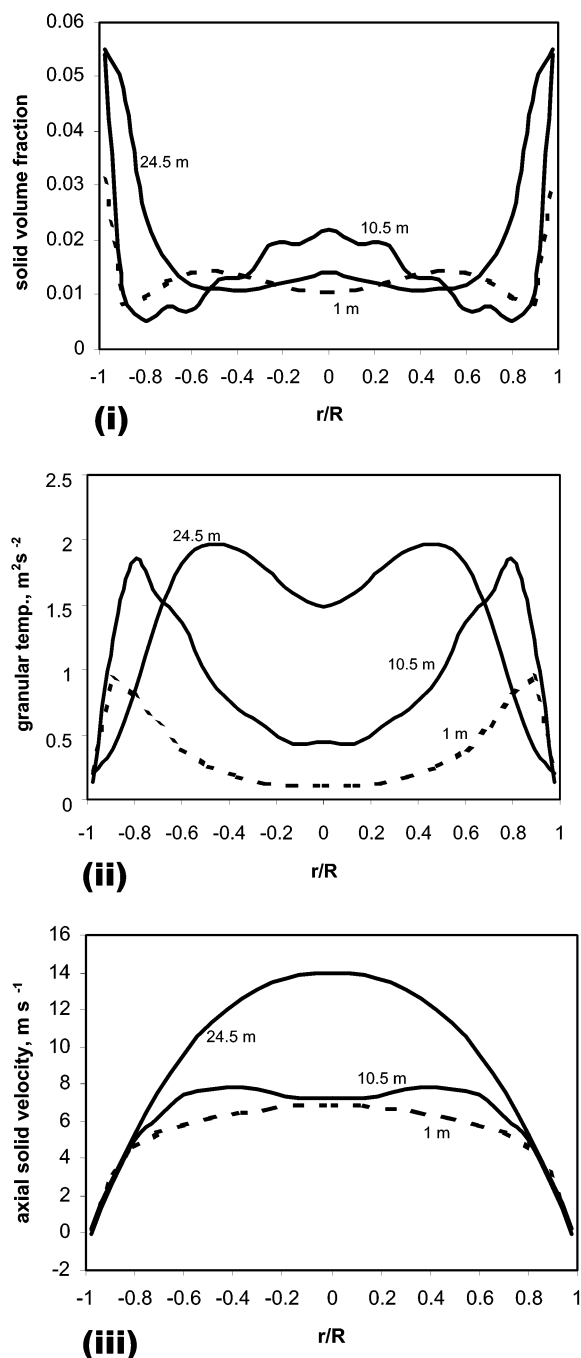
(i)

(ii)

(iii)

Figure 9. Radial variations of solid fraction, granular temperature, and solid velocity. Steady-state simulation. $G_s = 79.0$ kg m^{-2} s^{-1}; $u_g = 4.55$ m s^{-1}; $\theta_{in} = 0.14$ m^2 s^{-2}.

ity of the solid phase leading to an increase in the solid fraction. The latter is responsible for the localized decrease in the solid velocity (see Figure 8(i) and 9(iii)), at the middle level elevation in the riser. Similar observations of higher solid fraction in the core region were reported recently by Xu,[25] when measuring the catalyst density profile in a riser using γ-ray scanning. The radial variation of the catalyst density 5 m above the feed injection nozzle shows a core region of higher catalyst density as compared to a relatively dilute region at intermediate r/R. Interestingly, Xu[25] also indicates that the high-density core region becomes smaller when the gas velocity is increased by injecting additional steam. From the above, it may be concluded that such a high-density core region is mainly formed due to

inadequate gas velocity at intermediate solid fluxes, resulting in a localized low-turbulence region in the center of the riser.

In the top section of the riser, there is an increase in the gas/solid velocity due to an increase in the production of the lighter products, for example, gasoline, gas, and LPG. The increase in the velocity is also partly due to two other reasons: (i) a higher annulus thickness in the top section of the riser decreases the effective flow area significantly and (ii) the gas-phase pressure in the top section of the riser is lower than that at the bottom due to the hydrostatic head of the solid. A low pressure allows the gas to expand, thus increasing the solid velocity by the drag force.

Due to the above effects, the gas and solid velocities in the top section of the riser have an almost parabolic shape. A similar velocity profile is also reported by Landeghem et al.[24] in an experimental study of a cold flow setup with an average gas velocity of 6.7 m s^{-1} and solid flux of 303 kg m^{-2} s^{-1}.

The higher velocity leads to a corresponding increase in the granular temperature and the gas-phase turbulence k, as seen in Figure 8(iii),(iv).

Another important point to note is that the present 3D model is based on the kinetic theory of granular flow (KTGF[6]). The latter does not account as such for the mesophase fluctuations due to clustering, and even more so if the steady-state computation is used,[14] as in the present simulation. Despite this, the 3D model still predicts the radial segregation of the particles remarkably well. Furthermore, as shown later in the sections on radially averaged flow and reaction variables, the 3D model is also able to predict the slip factor and the radially averaged axial solid density profile, which are comparable, at least qualitatively, to the experimental data at similar conditions. This remarkable success of the KTGF approach implies that the particle-level fluctuations are indeed the dominating phenomena at least up to a moderate solid flux (<100 kg m^{-2} s^{-1}). This is also supported by the conclusion of Zheng et al.,[26] based on a simulation at a solid flux of 34 kg m^{-2} s^{-1}, that 75% of the solid-phase fluctuating energy is contributed by the particle-level fluctuation, whereas the remaining 25% is due to the mesophase clustering. However, when the solid flux is very high (500 kg m^{-2} s^{-1}), the clustering phenomena are expected to take a dominating role in the solid-phase turbulence.

Radial and Axial Variations of Reaction Variables

The radial variations of the reaction variables are shown in Figure 10. As can be expected, the conversion is higher near the wall than at the center, especially at the bottom of the riser. For example, the total heavy lumps show a concentration difference of about 0.1 weight fraction at an elevation of 1 m (Figure 10(i)). This is mainly due to a higher solid fraction near the wall (Figure 8(ii)) and also because the gas/solid velocities are lower near the wall (Figure 8(i)). However, the radial concentration profiles are somewhat flat, especially at the middle level elevation of the riser (Figure 10(iii), z = 10.5 m). The latter is partly due to the decrease in the concentration of the heavier fractions with riser height. It is also due to a relatively flat velocity at this elevation (Figure 8(i)). In fact, the solid fraction increases in the core region at z = 10.5 m (Figure 8(ii)). In addition, this is also due to the significant increase

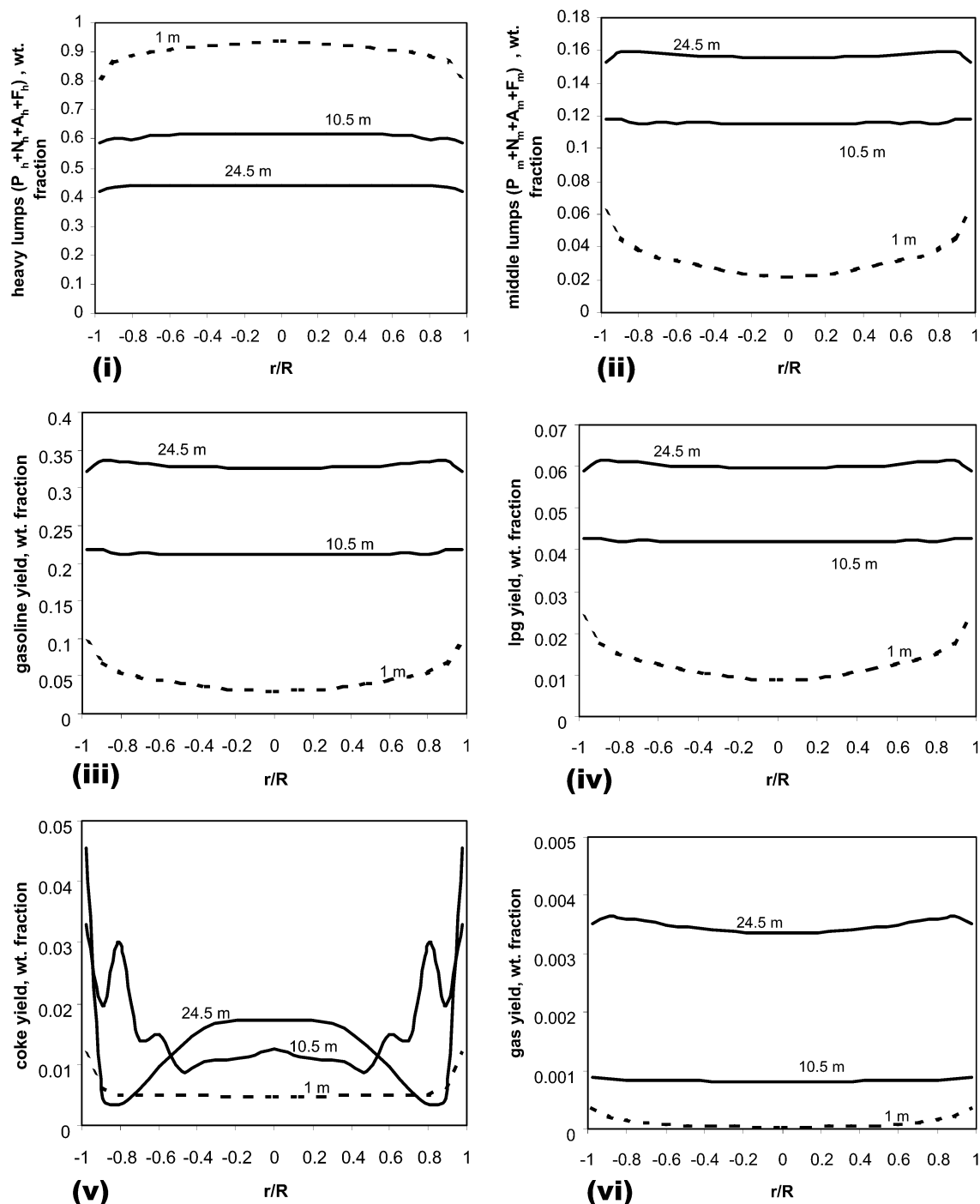**Figure 10.** Radial variations of reaction variables at three riser elevations: 1 m, 10.5 m, and 24.5 m. Steady-state simulation. $G_s = 79.0$ kg m^{-2} s^{-1}; $u_g = 4.55$ m s^{-1}; $\theta_{in} = 0.14$ m^2 s^{-2}; $d_p = 65$ μm; $D = 0.4$ m.

of the coke yield in the annulus section (Figure 10(v)). Another reason for the relatively flat radial concentration profiles is the turbulent diffusion of the gaseous components. The turbulent diffusivity ($\nu_g^t/\sigma_c = 0.09 k^2/\epsilon$) is found to be 0.008 and 0.04 m^2 s^{-1} at 4 and 18 m elevation, respectively, as compared to the experimentally determined values of about 0.002 m^2 s^{-1} (Landeghem et al.[24]). The relatively higher values of turbulent diffusivity in this work, especially at higher elevations, is attributed to the increased gas velocity. On the other hand, the radial differences in the lump concentrations are somewhat increased at $z = 24.5$ m (Figure 10(iii)), partly due to the higher solid fraction near the wall (Figure 8(ii)).

When comparing the reactivity of different heavy lumps (not shown), it is seen that the aromatic substituent lump A_h is highly reactive, leading to a very fast extinction. On the other hand, the reactivity of the aromatic ring lump F_h is quite low. Most of the middle distillate lumps have maximum yields somewhere in the middle in the riser, beyond which the overcracking increases, leading to an increase in the gasoline yield, LPG yield, and gas yield.

The coke yield (Figure 10(v)), on the other hand, shows some remarkable features. Generally, the coke yield is higher in the annulus region than in the core. This is expected since the residence time is lower in the annulus, allowing a higher conversion in this region.
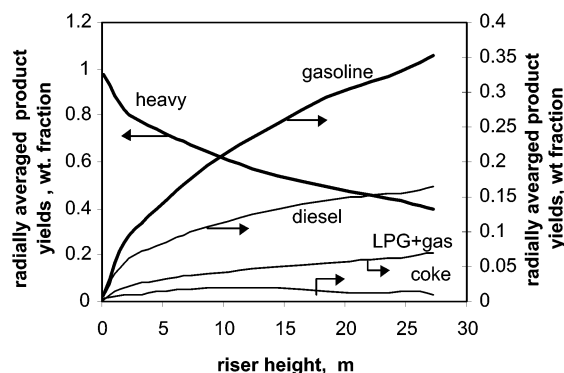
Figure 11. Radially averaged axial variations of yield. Steady-state simulation. $G_s = 79.0$ kg m^{-2} s^{-1}; $u_g = 4.55$ m s^{-1}; $\theta_{in} = 0.14$ m^2 s^{-2}; $d_p = 65$ μm; $D = 0.4$ m.

This indeed confirms that the conversion in the annulus region is higher. However, it is largely not reflected in the gas-phase radial component concentrations (Figure 10(i)−(iv)) due to the excellent mixing as a consequence of the gas-phase turbulence, as indicated before. The off-center peak in the coke yield at $r/R = 0.8$ and $z = 10.5$ m (see Figure 10(v)) is a result of the lower solid fraction at that point due to the higher granular temperature (Figure 8(iii)). However, in the top of the riser, the coke yield is higher in the core region than in the annulus. This is partly due to the carryover of coke from the annulus to the core region at a higher turbulence level (Figure 8(iv)) due to the turbulent radial dispersion of the solid as indicated by a higher granular temperature (Figure 8(iii)). In addition, since the major reactions are gasoline and middle distillate overcracking, the coke production rate is relatively low in the top section.

Finally, Figure 11 shows the radially averaged product yields. They qualitatively agree with the reported data of Martin et al.[7] and Landeghem et al.[24]

Radially Averaged Flow and Reaction Variables: Comparison with 1D Simulation Results

Radial Averaging Procedure for the 3D Simulation Data. The radial averaging of the variables has to reflect the significant radial variation of the mass flux for both gas and solid phases. Hence, for example, the radial average of the solid-phase velocity is obtained by integrating the mass flux and solid density over the surface area S in each horizontal cross section

$$v_{avg} = \frac{\int \epsilon_s \rho_{sp} \mathbf{v} \cdot \mathbf{n}\, dS}{\int \epsilon_s \rho_{sp}\, dS} \tag{33}$$

where $\mathbf{n}$ is the normal vector of the horizontal surface. Similarly, the radially averaged gas velocity is calculated from

$$u_{avg} = \frac{\int \epsilon_g \rho_g \mathbf{u} \cdot \mathbf{n}\, dS}{\int \epsilon_g \rho_g\, dS} \tag{34}$$

The radially averaged solid fraction is calculated from

$$\epsilon_{s,avg} = \frac{\int \epsilon_s \rho_{sp}\, dS}{\int \rho_{sp}\, dS} \tag{35}$$

and the radially averaged product yields from

$$Z_{j,avg} = \frac{\int Z_j\, dS}{\int dS} \tag{36}$$

where Z_j is defined by eq 32.

Note that the net mass flow rate summed up over the entire surface is equal to the multiplication of the average values ($\epsilon_{s,avg}\rho_{sp}v_{avg}S$). Furthermore, eq 35, which is based on the arithmetic average, represents the net solid density in the horizontal surface, which is experimentally measured from the axial pressure gradient data. On the other hand, the product yields are arithmetically averaged (see eq 36) since the radial variation of Z_j is not very significant in the major part of the riser (see Figure 10).

1D Model Description. A 1D model for reactive gas−solid flow that only considers axial variations of the variables was also used to perform a simulation of the FCC riser, both with and without taking clustering effects into account. It includes two momentum equations so as to be able to distinguish between gas- and solid-phase velocity.

As for concentration and temperature, the model is based on the pseudo-homogeneous assumption; both internal and external mass- and heat-transport resistances are neglected. In fact, from the results of the 3D simulation, the external mass-transport resistance was found negligible for the FCC riser. The latter is attributed to the relatively high solid fraction in the riser, providing a high external surface area for an efficient mass transport. By a similar reasoning, interphase heat transfer can be neglected as well, provided the temperature difference between gas and solid phase is not large. This assumption does not hold for the inlet region of the riser, due to the boundary conditions imposing a temperature difference of almost 200 °C, and therefore the 1D model is only applicable to the remaining part of the riser.

In addition, the diffusional and turbulent transport of mass, momentum, and heat are neglected in the 1D model.

Clustering Effects. The 1D model is able to take clustering effects into account to some extent, by basing the calculations on the effective cluster diameter instead of the single-particle diameter. The former is postulated to account for the clustering phenomena in the riser, which result from the interaction of drag force, gravity, and momentum of particles. The clustering of particles is a result of the localized loss of granular temperature due to the inelastic collision of particles or due to the damping of the fluctuating motion of the particles by the fluid.[27] The effective cluster diameter is calculated from[14]

$$L_{cl} = \sqrt{\frac{\mu_s v_t}{\rho_s g_z}} \tag{37}$$

and amounts to 0.15 cm based on the solid-phase viscosity estimated from[15]

$$\mu_s = \mu_s^c + \frac{\mu_s^k\left(1 + \frac{8}{5}\frac{(1 + e)}{2}\epsilon_g g\right)\left(1 + \frac{8}{5}\epsilon_s g\right)}{\epsilon_s g} \quad (38)$$

with

$$\mu_s^c = \frac{4}{5}\epsilon_s \rho_s d_p g(1 + e)\sqrt{\frac{\theta}{\pi}} \quad (39)$$

$$\mu_s^k = 1.016\frac{5}{16}\frac{m}{d_p^2}\sqrt{\frac{\theta}{\pi}} \quad (40)$$

and the granular temperature corresponding to a value of 0.17 m^2 s^{-2}. The latter is based on a typical averaged value obtained from the 3D simulation.

1D model equations:

Continuity equation for the gas phase

$$\frac{d}{dz}(\epsilon_g \rho_g u) = (1 - \epsilon_g)\rho_p \sum_j \mathcal{R}_j M_j \quad (41)$$

Momentum equation for the gas phase

$$\frac{d}{dz}(\epsilon_g \rho_g u^2) = -\epsilon_g \frac{dP}{dz} - \beta(u - v) + F_{w,g} - \epsilon_g \rho_g g \quad (42)$$

Component continuity equation in gas phase

$$\frac{d}{dz}(\epsilon_g C_j u) = (1 - \epsilon_g)\rho_p \mathcal{R}_j \quad (43)$$

Continuity equation for the solid phase

$$\frac{d}{dz}((1 - \epsilon_g)\rho_{sp} v) = -(1 - \epsilon_g)\rho_p \sum_l \mathcal{R}_l M_l \quad (44)$$

Momentum equation for the solid phase

$$\frac{d}{dz}((1 - \epsilon_g)\rho_{sp} v^2) = -(1 - \epsilon_g)\frac{dP}{dz} + \beta(u - v) + F_{w,s} - (1 - \epsilon_g)\rho_{sp}g \quad (45)$$

Component continuity equation in solid phase

$$\frac{d}{dz}((1 - \epsilon_g)\rho_{sp}\theta_l v) = (1 - \epsilon_g)\rho_{sp}\mathcal{R}_l \quad (46)$$

An overall enthalpy balance, eq 47, is included in the 1D model to calculate the temperature drop due to the endothermicity of the cracking reactions. In this equation, T represents the temperature that the gas and solid phase share (by virtue of the assumption of pseudo-homogeneity in temperature).

Energy equation

$$\frac{d}{dz}(\epsilon_g \rho_g u c_{p,g} T) + \frac{d}{dz}((1 - \epsilon_g)\rho_{sp} v c_{p,s} T) = \sum_p (1 - \epsilon_g)\rho_p(-\Delta H_p)r_p \quad (47)$$

Results and Discussion

In Figure 12, the results for the 3D and 1D simulations are compared both for flow and reaction variables.

In Figure 12(i), it is seen that the radially averaged solids volume fraction varies in a nonlinear manner with riser height. At the riser bottom, the solid density is higher due to the initial acceleration effect of the solid. The latter results from the lower inlet velocity of the solid (Table 2), which implies a higher solid fraction for a specified solid mass flux. However, the solid is quickly accelerated due to the drag force exerted by the gas, resulting in a decrease in the solid fraction. At higher elevations, the radially averaged solid density as predicted by the 3D model again increases due to the outlet effect. Since the present simulation has two abrupt T-type side outlets, there is a considerable densification near the outlet. A similar increase in the solid density near the outlet is experimentally observed by Martin et al.[7] as well. The solid density sharply decreases above the outlets due to the lower solid flux. Furthermore, it is seen that the 1D model without clustering consistently predicts a lower solid fraction as compared to the 3D model. Similarly, the axial solid velocity is significantly overpredicted while the slip velocity and the slip factor are severely underpredicted by this model (Figure 12(ii)−(iv)). In fact, in the 1D model, the slip velocity is almost constant and equal to the single-particle terminal velocity v_t, which amounts to about 0.15 m s^{-1} for FCC particles. On the other hand, the slip velocity in the 3D model is 5−20 times the terminal velocity of a single particle. This leads to the relatively lower solid velocity and, hence, the higher slip factor based on the radial averaging of the mass flux (eqs 33 and 34). The increase in the slip velocity in the upper part of the riser is attributed to the effect induced by the abrupt T-type outlet geometry. However, at an elevation of 25 m, that is, above the outlets, the slip velocity shows a dramatic drop (Figure 12(iii)). This is mainly attributed to the fact that the majority of the gas is quickly released through the outlets, whereas the solid particles continue to move upward due to inertia. Hence, although the solid velocity decreases above 25 m (Figure 12(ii)), the decrease in the gas velocity is even higher, resulting in a dramatic drop of the slip velocity above the outlets. Despite a significant variation in the slip velocity throughout the riser, the slip factor varies over a surprisingly narrow range of 1.5−2, which matches qualitatively with the observation of Matsen.[28]

The lower slip factor for the 1D model without clustering also results in a lower solid fraction in the riser. The latter is responsible for a lower conversion as observed from the higher amount of unconverted hydrocarbons (Figure 12(v)) and the lower gasoline yield (Figure 12(vi)) for the 1D model without clusters. On the other hand, the 1D model with clustering predicts a higher slip velocity due to the higher terminal velocity v_t for bigger diameter clusters (0.15 cm). However, the solid fraction, slip velocity, and slip factor are considerably overpredicted by the model as compared to the 3D results. Consequently, the unconverted heavy fraction is lower and the gasoline yield is higher with this model, at least for the major part of the riser. The slip velocity is considerably underpredicted in the 1D model without clusters because the nonuniform radial distribution is completely neglected. In addition, the effect of the outlet geometry cannot be accounted for if a 1D model is used. Although the use of an effective cluster diameter alleviates the problem of the underprediction of slip velocity, it results in an unusually higher solid fraction in most of the riser due to the assumption of radial uniformity. The gasoline yield and the unconverted fractions predicted by the cluster model are quite comparable with
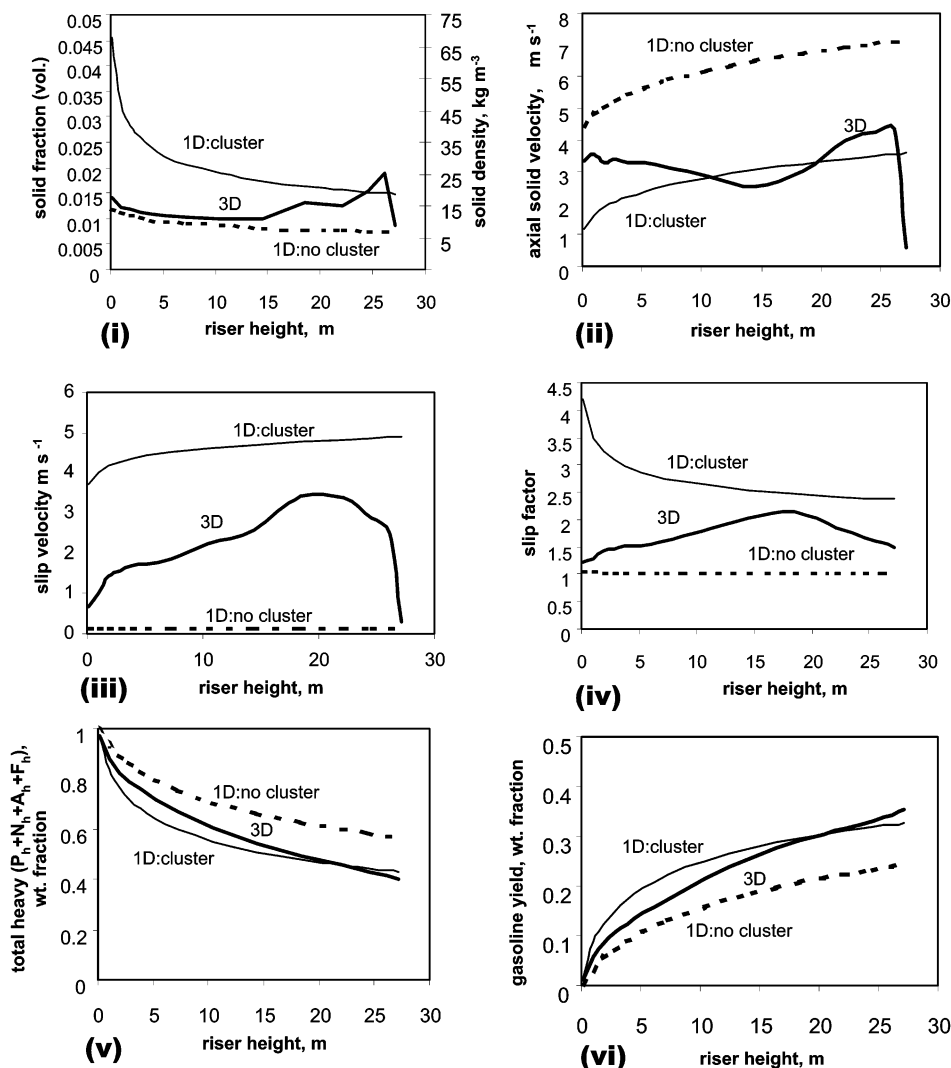
Figure 12. Comparison of 3D and 1D simulation results: axial variations of flow and reaction variables. "1D: no cluster" implies the 1D simulation without considering particle clustering. "1D: cluster" implies the prediction was obtained using a cluster diameter of 0.15 cm. G_s = 79.0 kg m^{-2} s^{-1}; u_g = 4.55 m s^{-1}; θ_{in} = 0.14 m^2 s^{-2}; d_p = 65 μm; D = 0.4 m.

those of the 3D model and the plant data. Although the final yields at the riser exit are of primary interest, the axial and radial variations of the flow and reaction variables are equally important, especially for a reliable design and scale-up. Hence, the importance of the 3D simulation to adequately simulate the complex hydrodynamic behavior of the gas−solid riser flow is demonstrated.

Conclusions

A 3D simulation of an industrial-scale FCC riser reactor is performed using the novel density-based solution algorithm. This algorithm was found to provide a stable and reliable simulation, but the strong coupling of flow and reaction variables needs to be further addressed. The particle-level fluctuations are modeled using the kinetic theory of granular flow. The kinetic scheme is based on a 12-lump model including coke as a separate lump. Both the flow and reaction fields are solved using the steady-state computational mode. This implies that the mesophase fluctuations of the solid due to clustering are not accounted for as such. The kinetic theory of granular flow (KTGF) was found to simulate the riser hydrodynamics adequately, at least up to a moderate solid flux of 80 kg m^{-2} s^{-1} in the present test

case as compared to solid fluxes of 500 kg m^{-2} s^{-1} in a typical FCC unit.

The results also show a significant radial nonuniformity of the flow and reaction fields. The gas−solid flow resembles a core annular pattern. There is a major increase in the annulus thickness near the top of the riser due to the abrupt T-outlet. This is in line with experimental findings reported in the literature. A considerable gas−solid slip amounting to an average slip factor of about 2 is calculated in the 3D simulation. Similar values of the slip factor under FCC conditions are reported in the literature. The higher slip factor in the 3D model is a direct outcome of the significant radial nonuniformity of the solid fraction and solid velocity. The accurate prediction of the radial profiles and of the slip factor by the 3D model proves that the particle level fluctuations, as accounted by the KTGF formulation, play a dominating role in the overall fluctuations of the solid-phase velocity, at least up to moderate solid fluxes.

A comparison of the 3D and 1D simulation shows that the 1D model is unable to account for the gas−solid slip adequately. The radially uniform profiles result in an overall decrease in the solid fraction and the residence time of the solid in the riser, which in turn results in a significant underprediction of the conversion. A 1D

model using an effective cluster diameter instead of the single-particle diameter predicts product yields comparable to those of the 3D simulation, but results in unreasonably high slip factors.

Acknowledgment

List of Symbols

$A_{i/i'}^{(m)}$ = symbolic flux coefficient for current/surrounding grid point(s)

$\tilde{A}_i^{(m)}$ = coefficient matrix for grid point i with values evaluated at pseudo-time level m

a_m = external particle surface area per unit mass of solid, $m_p^2\ kg_{solid}^{-1}$

a_v = external particle surface area per unit reactor volume, $m_p^2\ m_r^{-3}$

$\tilde{B}_i^{(m)}$ = right-hand side vector for grid point i with values evaluated at pseudo-time level m

$\mathbf{C}$ = random fluctuating velocity of an individual particle, $m\ s^{-1}$

$C_{1\epsilon}, C_{2\epsilon}, C_{4\epsilon}$ = turbulence model parameters, dimensionless

C_c = coke content of catalyst, $kg\ kg^{-1}$

C_g = speed of sound for the gas phase, $m\ s^{-1}$

C_j = gas-phase concentration of component j, $mol\ m_{gas}^{-3}$

C_t = site capacity of the catalyst, $mol_{site}\ kg_{cat}^{-1}$

c_p = heat capacity, $J\ kg^{-1}\ K^{-1}$

D = riser diameter, m

D_m = mean molecular diffusivity of the gas mixture, $m^2\ s^{-1}$

d_p = particle diameter, m

E_g = gas-phase total energy, $J\ kg^{-1}$

E_p = activation energy for reaction path p, eq 17, $J\ mol^{-1}$

e = restitution coefficient of particles, dimensionless

e_{sp} = solid-phase internal energy, $J\ kg^{-1}$

F_w = volumetric wall friction force, $N\ m^{-3}$

G_s = solid mass flux, $kg\ m^{-2}\ s^{-1}$

g = radial distribution function, eqs 38–40, dimensionless

$\mathbf{g}, g_z$ = gravity vector, z-component of gravity vector, $m\ s^{-2}$

H = riser height, m

$-\Delta H_p$ = heat of reaction, path p, $J\ mol^{-1}$

$\mathbf{h}$ = energy flux for conductive transport of granular temperature, $kg\ s^{-3}$

h_f = interphase heat-transfer coefficient, $J\ m_p^{-1}\ s^{-1}\ K^{-1}$

h_{mj} = molar enthalpy of component j, $J\ mol_j^{-1}$

$\mathbf{I}$ = unit tensor

i = grid point i

i' = surrounding grid points

k = turbulent kinetic energy of gas phase, $m^2\ s^{-2}$

k_{gj} = mass-transfer coefficient of component j, $mol\ m^{-2}\ s^{-1}$

k_p = reaction rate coefficient for reaction path p, $m^3\ kg_{cat}^{-1}\ s^{-1}$

$M_{j/l}$ = molecular mass of component j/species l, $kg\ mol^{-1}$

m = mass of one solid particle in eq 40, kg

$\mathbf{n}$ = normal vector

P = gas-phase static pressure, $N\ m^{-2}$

P_s = solid-phase pressure, $N\ m^{-2}$

$\mathbf{Q}$ = set (vector) of conservative variables

$\Delta\mathbf{Q}$ = correction vector for the conservative variables

q_{12} = gas–solid turbulence correlation, $m^2\ s^{-2}$

q_s = mean kinetic energy of solid phase, $m^2\ s^{-2}$

$\mathcal{R}_{j/l}$ = net production rate of component j/species l, $mol\ kg_{cat}^{-1}\ s^{-1}$

r_p = reaction rate for path p, $mol\ kg_{cat}^{-1}\ s^{-1}$

S = surface area, m^2

$\mathbf{S}$ = vector of source terms, eq 21

$\mathbf{s}_g^m$ = viscous stress tensor for the gas phase, $kg\ m^{-1}\ s^{-2}$

$\mathbf{s}_g$ = total gas-phase stress tensor, $kg\ m^{-1}\ s^{-2}$

$\mathbf{s}_s$ = total solid-phase stress tensor, $kg\ m^{-1}\ s^{-2}$

T = gas-phase temperature, K

T = common gas- and solid-phase temperature in eq 47, K

t = (real) time, s

Δt = (real) time step, s

U_r = reference velocity for preconditioning, $m\ s^{-1}$

$\bar{\mathbf{u}}$ = time-smoothed hydrodynamic velocity vector of the gas phase, $m\ s^{-1}$

u = 1D gas-phase velocity, $m\ s^{-1}$

$\mathbf{v}$ = instantaneous, locally averaged hydrodynamic velocity vector of the solid phase, $m\ s^{-1}$

v = 1D solid-phase velocity, $m\ s^{-1}$

v_t = terminal velocity of a single particle, $m\ s^{-1}$

$\mathbf{W}$ = set (vector) of primary variables

W_j = weight fraction of component j in the gas, dimensionless

$\mathbf{x}$ = position vector in Cartesian system, m

$\Delta x, \Delta y, \Delta z$ = grid size in x,y,z-direction, m

Y_j = mole fraction of component j, dimensionless

Z_j = weight fraction of component j with respect to all hydrocarbons (thus including coke, which resides in the solid phase), dimensionless

z = axial coordinate, m

Greek Notations

α = scaling factor, dimensionless

β = interphase momentum-transfer coefficient, $kg\ m_{reactor}^{-3}\ s^{-1}$

$\mathbf{\Gamma}$ = preconditioning matrix

γ = dissipation of kinetic fluctuation energy of the solid phase by inelastic particle–particle collisions, $kg\ m^{-1}\ s^{-3}$

γ = ratio of heat capacities, c_p/c_v, eq 30, dimensionless

γ_{jp} = stoichiometric factor of lump j in reaction path p, dimensionless

ϵ = dissipation of turbulent kinetic energy of the gas phase (without subscript), $m^2\ s^{-3}$

ϵ = volume fraction (with subscript), dimensionless

ϵ_{12} = dissipation of turbulence correlation, $m^2\ s^{-3}$

Θ_l = coverage of species l, $\Theta_l = \theta_l C_t$, $mol_l\ kg_{cat}^{-1}$

θ = granular temperature, $m^2\ s^{-2}$

θ_l = fractional coverage of species l, $mol_l\ mol_{site}^{-1}$

κ = granular conductivity of the solid phase, $kg\ m^{-1}\ s^{-1}$

λ = conductivity, $J\ m^{-1}\ K^{-1}\ s^{-1}$

μ = shear viscosity, $kg\ m^{-1}\ s^{-1}$

ν_{12} = kinematic viscosity of turbulence correlation, $m^2\ s^{-1}$

ν_g^t = kinematic turbulent viscosity of gas phase, $m^2\ s^{-1}$

ξ = bulk viscosity, $kg\ m^{-1}\ s^{-1}$

ρ = density, $kg\ m^{-3}$

$\sigma_{k;\epsilon;q;s;c;\Theta}$ = eddy parameters

τ = pseudo-time, s

$\Delta\tau$ = pseudo-time step, s

ϕ = flux vector

φ_c = coke deactivation function, dimensionless

Additional Notations

$^-$ = time-smoothed mean

$'$ = fluctuating part

bold letters, e.g., $\mathbf{C}$, = vector

Superscripts

c = collisional contribution (to viscosity), eqs 38–40

k = kinetic contribution (to viscosity), eqs 38–40

(m) = denotes value at pseudo-time level m

s = inside solid phase

T = transpose matrix
t = turbulent
(t) = denotes value at (real) time t

Subscripts

avg = average
g = gas phase
j = component in gas phase
l = species in solid
p = reaction path
s = solid sorbent/catalyst
sp = solid phase including species, coke, etc.
w = wall

Literature Cited

(1) Weekman, V. W., Jr.; Nace, D. M. Kinetics of Catalytic Cracking Selectivity in Fixed, Moving and Fluid Bed Reactors. *AIChE J.* **1970**, *16*, 397.

(2) Jacob, S. M.; Gross, B.; Voltz, S. E.; Weekman, V. W., Jr. A Lumping and Reaction Scheme for Catalytic Cracking. *AIChE J.* **1976**, *22*, 701.

(3) Froment, G. F. Fundamental Kinetic Modeling of Complex Processes. In *Chemical Reactions in Complex Mixtures—the Mobil Workshop*; Sapre, A. V., Krambeck, F. J., Eds.; Van Nostrand Reinhold: New York, 1991.

(4) Kwauk, M.; Wang, N.; Li, Y.; Chen, B.; Shen, Z. Fast Fluidization at ICM. In *Circulating Fluidized Bed Technology*; Basu, P., Ed.; Pergamon: Toronto, Ontario, 1986.

(5) Kunii, D.; Levenspiel, O. Flow Modeling of Fast Fluidized Beds. In *Circulating Fluidized Bed Technology III*; Basu, P., Horio, M., Hasatani, M., Eds.; Pergamon Press: New York, 1991.

(6) Gidaspow, D. *Multiphase Flow and Fluidization: Continuum & Kinetic Theory Descriptions*; Academic Press: San Diego, CA, 1994.

(7) Martin, M. P.; Derouin, C.; Turlier, P.; Forissier, M.; Wild, G.; Bernard, J. R. Catalytic Cracking in Riser Reactors: Core-Annulus and Elbow Effects. *Chem. Eng. Sci.* **1992**, *47*, 2319.

(8) Wong, R.; Pugsley T.; Berruti, F. Modeling the Axial Voidage Profile and Flow Structure in Risers of Circulating Fluidized Beds. *Chem. Eng. Sci.* **1992**, *47*, 2301.

(9) Gao, J.; Xu, C.; Lin, S.; Yang, G.; Guo, Y. Advanced Model for Turbulent Gas–Solid Flow and Reaction in FCC Riser Reactors. *AIChE J.* **1999**, *45*, 1095.

(10) Theologos, K. N.; Markatos, N. C. Advanced Modeling of Fluid Catalytic Cracking Riser-Type Reactors. *AIChE J.* **1993**, *39*, 1007.

(11) De Wilde, J.; Heynderickx, G. J.; Vierendeels, J.; Dick, E.; Marin, G. B. An extension of the preconditioned advection upstream splitting method for 3D two-phase flow calculations in circulating fluidized beds. *Comput. Chem. Eng.* **2002**, *26*, 1677.

(12) Merkle, C. L.; Venkateswaran, S.; Buelow, P. E. O. The Relationship Between Pressure-Based and Density-Based Algorithms. AIAA 30th Aerospace Sciences Meeting, Reno, NV, January 6-9, 1992; *AIAA Paper No.* 92–0425.

(13) Simonin, O. Combustion and Turbulence in Two-Phase Flows. In *Continuum Modeling of Dispersed Two-Phase Flows*; von Karman Institute for Fluid Dynamics: Brussels, 1996; Lecture Series no. 1996–02.

(14) Agrawal, K.; Loezos, P. N.; Syamlal, M.; Sundaresan, S. The Role of Meso-Scale Structures in Rapid Gas–Solid Flows. *J. Fluid. Mech.* **2001**, *445*, 151.

(15) Nieuwland, J. J.; van Sint Annaland, M.; Kuipers, J. A. M.; van Swaaij, W. P. M. Hydrodynamic Modeling of Gas Particle Flows in Riser Reactors. *AIChE J.* **1996**, *42*, 1569.

(16) Peixoto, F. C.; de Medeiros, J. L. Reactions in Multi-indexed Continuous Mixtures: Catalytic Cracking of Petroleum Fractions. *AIChE J.* **2001**, *47*, 935.

(17) Martignoni, W.; de Lasa, H. I. Heterogeneous Reaction Model for FCC Riser Units. *Chem. Eng. Sci.* **2001**, *56*, 605.

(18) Das, A. K.; Van engelandt, G.; Marin, G. B.; Heynderickx, G. J. Transient 3D Simulation of the turbulent gas–solid flow in large scale risers using a density based solution algorithm. *ASME 2002, Proceedings of the 4th International Symposium on Computational Technologies for Fluid-Thermal-Chemical Systems with Industrial Applications*, Vancouver, Canada, 2002.

(19) De Wilde, J. Adsorption of SO_2 and NO_x in a riser: kinetics and 3D gas–solid hydrodynamics. Ph.D. Dissertation, Ghent University, Ghent, 2000.

(20) Weiss, J. M.; Smith, W. A. Preconditioning Applied to Variable and Constant Density Flows. *AIAA J.* **1995**, *33*, 2050.

(21) van der Schaaf, J.; Schouten, J. C.; van den Bleek, C. M. Origin, propagation and attenuation of pressure waves in gas–solid fluidized beds. *Powder Technol.* **1998**, *95*, 220.

(22) Godfroy, L.; Patience, G. S.; Chaouki, J. Radial Hydrodynamics in Risers. *Ind. Eng. Chem. Res.* **1989**, *38*, 81.

(23) Sun, B.; Gidaspow, D. Computation of Circulating Fluidized-Bed Riser Flow for the Fluidization VIII Benchmark Test. *Ind. Eng. Chem. Res.* **1999**, *38*, 787.

(24) Van Landeghem, F.; Nevicato, D.; Pitault, I.; Forissier, M.; Turlier, P.; Derouin, C.; Bernard, J. R. Fluid Catalytic Cracking: Modelling of an Industrial Riser. *Appl. Catal. A–Gen. 138*, 381.

(25) Xu, S. X. Optimizing FCC Risers by CAT-Scan. *Tru-News* **2002**, *10*, Vol. 10, ed. 1.

(26) Zheng, Y.; Wan, X.; Qian, Z.; Wei, F.; Jin, Y. Numerical Simulation of the Gas–Particle Turbulent Flow in Riser Reactor based on $k–\epsilon–k_p–\epsilon_p–\Theta$ Two-Fluid Model. *Chem. Eng. Sci.* **2001**, *56*, 6813.

(27) Wylie, J. J.; Koch, D. L. Particle Clustering due to Hydrodynamic Interactions. *Phys. Fluids* **2000**, *12*, 964.

(28) Matsen, J. M. Some Characteristics of Large Solid Circulation Systems. In *Fluidization Technology*; Keairns, D. L., Ed.; Hemisphere: New York, 1976.